

Computational time-of-flight diffuse optical tomography

Ashley Lyons¹, Francesco Tonolini², Alessandro Boccolini³, Audrey Repetti⁴, Robert Henderson⁵, Yves Wiaux⁴ and Daniele Faccio^{1*}

Imaging through a strongly diffusive medium remains an outstanding challenge, in particular in applications in biological and medical imaging. Here, we propose a method based on a single-photon time-of-flight camera that allows, in combination with computational processing of the spatial and full temporal photon distribution data, imaging of an object embedded inside a strongly diffusive medium over more than 80 transport mean free paths. The technique is contactless and requires 1 s acquisition times, thus allowing Hz frame rate imaging. The imaging depth corresponds to several centimetres of human tissue and allows us to perform deep-body imaging as a proof of principle.

Visible or near-infrared (NIR) light propagating in turbid media, for example biological tissue or a foggy environment, follows a complicated random path due to multiple scattering. As a consequence, the optical wavefront is severely modified and its intensity is rapidly attenuated in propagation. This leads to the inability of an imaging system to detect an object that is located within and thus obscured by the medium. Recent efforts have also been directed at imaging objects that are located behind or embedded in a scattering medium^{1–3}.

Generally speaking, photons propagating in a scattering medium can be divided into ballistic, snake and diffusive photons⁴. Ballistic and snake photons propagate with no or very little interaction with the scatterers along the direction of the beam. They therefore retain their original coherence and most of the image information. However, they are also exponentially suppressed and do not survive beyond distances of several centimetres in biological or highly scattering tissue. A medium of thickness L is considered to be highly diffusive when the transport mean free path $\ell^* = 1/\mu_s' \ll L$, where μ_a and μ_s' are the absorption and reduced scattering coefficients, respectively^{4–8}, with typical values for biological tissue that are of order $\mu_a \approx 0.05 \text{ cm}^{-1}$ and $\mu_s' \sim 10 \text{ cm}^{-1}$ ($\ell^* \sim 0.1 \text{ cm}$)⁹. The transport mean free path represents the distance over which all information on the photon's initial propagation direction is lost. Measurements of light transmitted through such a material therefore carry very little or no direct image information. Here we focus attention on this propagation regime.

The first generation of experiments and methods for diffuse imaging were developed in the late 1980s and early 1990s, establishing the boundaries in terms of maximum imaging depth and resolution^{10–14}. Successive generations were aimed at medical tests in a variety of conditions and also in vivo^{15–20}. The aim of most studies in recent years has been towards increasing image contrast, depth sensitivity and decreasing acquisition times^{7,21–23}.

In the strongly diffusive regime, light will propagate in the form of photon density waves (PDWs), which exhibit many features typical of standard propagating waves, including interference, diffraction and also imaging properties. Imaging properties are essentially determined by the wavevector associated to PDWs, $\kappa_d = \sqrt{3\mu_s'/\ell^*}$

(ref. 5). For typical biological tissue, $\kappa_d \approx 1 \text{ cm}^{-1}$, thus limiting imaging resolution to transverse dimensions that are of the same order of magnitude of the medium thickness; for example, spatial resolutions of the order of 5 cm are achieved in 5-cm-thick samples^{6,24}. This can be improved by using computational techniques, for example inverse retrieval algorithms⁵, or by post-selecting data in the temporal domain²⁵ to achieve resolutions of $\sim 1 \text{ cm}$ with realistic scattering parameters. We note that, in the latter case, the majority of the temporal information was discarded to filter out data only at one specific temporal slice where the spatial resolution was found to be highest.

Combining computational-based time-resolved measurements with ultrafast imaging has been shown to be a promising technique for retrieving information lost in a highly scattering medium; see, for example, ref. 6 for a review. An approach has been introduced that builds on all of the temporally resolved data, named ‘all photons imaging’ (API). API utilizes both spatial and temporal (photon arrival time) components of scattered light and has been successfully demonstrated to improve the spatial resolution of an object hidden behind a turbid medium²⁶.

In all the methods outlined above, the acquired data (images at the output plane of the scattering medium) show a clear shadow cast by the hidden object that is always clearly visible, even in the time-integrated image. The effect of the computational methods, including API, is to significantly improve the spatial resolution of the acquired image. Pioneering work was performed by Cai and colleagues in which the position of 5-mm-sized objects embedded within 60 mm of diffusive medium (2.5 mm transport mean free path) was determined using fibre source/detector pairs and a streak camera²⁷.

Here we introduce a time-of-flight diffusive optical tomography (ToF-DOT) approach to address the problem of imaging an object deeply embedded inside a highly scattering medium. Unlike the aforementioned methods, we investigate a regime where any signatures, even of the presence of an occluding object within the scattering medium, are too weak to be identified from visual inspection of the raw data alone. We use the full spatial and temporal information of the photon time-of-flight at each pixel spatial position recorded on a single-photon array detector in combination with

¹School of Physics and Astronomy, University of Glasgow, Glasgow, UK. ²School of Computing Science, University of Glasgow, Glasgow, UK. ³Institute of Photonics and Quantum Sciences, Heriot-Watt University, Edinburgh, UK. ⁴Institute of Sensors, Signals and System, Heriot-Watt University, Edinburgh, UK. ⁵Institute for Micro and Nano Systems, University of Edinburgh, Edinburgh, UK. *e-mail: daniele.faccio@glasgow.ac.uk

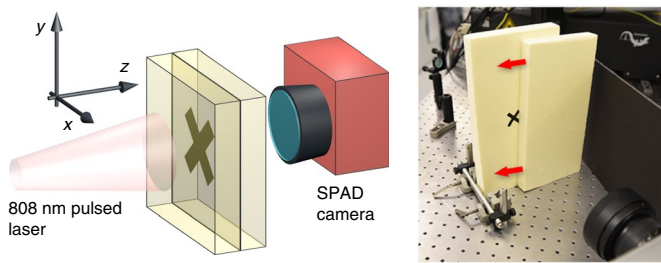


Fig. 1 | Experimental set-up. Layout (left) and photograph (right) of the experimental layout. The input laser beam is defocused to a diameter of ~5 cm and is centred on the embedded target (shapes cut out of black tape). A SPAD camera (visible also in the bottom right-hand corner of the photograph) is placed on the opposite side of the diffusive slabs to collect the transmitted laser light.

a computational retrieval method to estimate the hidden object shape and position. The ToF-DOT approach allows us to recover the shape of a two-dimensional (2D) opaque object hidden inside more than 80 transport mean-free-path lengths of diffusive material (corresponding to several centimetres of human tissue). We reconstruct millimetre-sized features and find that both the spatial and temporal resolution of the camera are key to achieving these results. Moreover, the technique is sufficiently sensitive to allow data acquisition on timescales of the order of 1 s.

Experimental set-up

We aim to reconstruct the shape and location of a 2D object embedded within a diffusive medium by performing spatially and temporally resolved intensity measurements of femtosecond light pulses transmitted through the medium. Our experimental set-up is illustrated in Fig. 1. We use a pulsed laser source with a wavelength of 808 nm, 120 fs temporal pulse duration, 80 MHz repetition rate and 1 W average power defocused to a spot size with a radius of 2.5 cm, thus corresponding to an illumination fluence of 0.5 mW mm^{-2} . This illuminates an object inside a medium consisting of two slabs of polyurethane foam, each 2.5 cm thick, with absorption and reduced scattering coefficients at the illumination wavelength measured from a single point, time-resolved measurement to be $\mu_a = 0.09 \text{ cm}^{-1}$ and $\mu'_s = 16.5 \text{ cm}^{-1}$ (see Methods for details). The material thus has a transport mean free path of $\ell^* = 600 \mu\text{m}$, that is, nearly two orders of magnitude smaller than the total thickness of the material, $L = 5 \text{ cm}$.

The laser pulses are transmitted through the diffusive medium and some of the light is absorbed by a hidden object placed between the two slabs. Black tape is used to create hidden targets of different shapes, for example letters (A, X), triangles or double lines. The transmitted light is collected by a camera composed of a 32×32 array of single photon avalanche diode (SPAD) detectors (commercialized by Photon Force), each operating in time correlated single photon counting (TCSPC) mode with 55 ps resolution²⁸. The SPAD camera therefore collects 3D data: two spatial dimensions with $N \times N = 32 \times 32$ pixel resolution and one temporal dimension ($T = 230 \times 55 \text{ ps}$ time bins).

The first column in Fig. 2 shows typical examples of time-integrated transmission images measured with the camera for various objects with feature sizes of order ~1 cm (shown in the last column). We also show time-gated images in the third column, attempting to isolate any eventual ballistic photons. The notable feature of these images is that in none of these is it possible to visually determine the presence (or absence) of an object embedded inside the medium.

Computational retrieval model

As noted above, the material has a transport mean free path $\ell^* = 600 \mu\text{m}$ that is two orders of magnitude smaller than the total

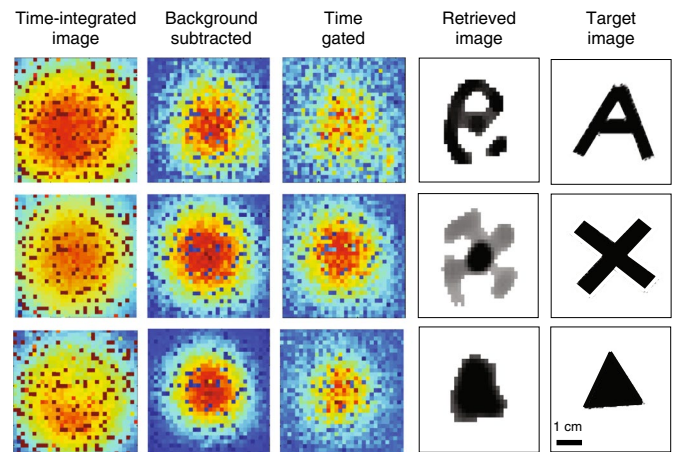


Fig. 2 | Main experimental results. The first column shows the object hidden inside the scattering medium. The second and third columns show the recorded image of the transmitted laser beam and time-gated on the first 10 time bins that are above the noise level, respectively. No discernible image is visible, showing that time-gating in an attempt to isolate ballistic photons is not successful. The fourth column shows the retrieved object images using the technique described in the main text. The fifth column shows the original unknown objects (dark pixels correspond either to dead pixels or to so-called ‘screamers’, that is, defected pixels with abnormally high dark counts).

thickness of the material. This places light in the strongly diffusive regime, which in turns allows us to model the photon propagation inside the diffusive medium using a diffusion approximation²⁹. Light within the medium essentially behaves like heat, following the steepest descent of the scalar gradient weighted by the diffusivity, with an additional loss effect due to photon absorption³⁰. The diffusion equation in the context of photon diffusion is expressed as

$$c^{-1} \frac{\partial \Phi(\mathbf{r}, t)}{\partial t} + \mu_a \Phi(\mathbf{r}, t) - D \nabla \cdot [\nabla \Phi(\mathbf{r}, t)] = S(\mathbf{r}, t) \quad (1)$$

where c is the speed of light in the medium, \mathbf{r} is the spatial position, t is the temporal coordinate, $\Phi(\mathbf{r}, t)$ is the photons flux, $S(\mathbf{r}, t)$ is a photon source and D is a term that includes the absorption coefficient μ_a and the reduced scattering coefficient μ'_s and in this work does not depend on \mathbf{r} or t : $D = (3(\mu_a + \mu'_s))^{-1}$. A full derivation of equation (1) beginning with the radiative transfer equation is provided in ref.³⁰. For the case of a highly localized (in space and time) input laser pulse, equation (1) has an analytical solution given by ref.¹¹:

$$\Phi(\mathbf{r}, t; \mathbf{r}', t') = \frac{c}{[4\pi Dc(t-t')]^{3/2}} \times \exp\left[-\frac{|\mathbf{r}-\mathbf{r}'|^2}{4Dc(t-t')}\right] \exp[-\mu_a c(t-t')] \quad (2)$$

Here, \mathbf{r}' and t' identify the position and time of the input laser pulse. Equation (2) describes the evolution of a delta function in time and can be applied to an extended light source (see Methods).

The image-retrieval model can be described as an inverse problem, where the aim is to estimate the shape of the hidden object $x \in \mathbb{R}^{N \times N}$, from the 3D (two spatial dimensions and one temporal dimension) observation obtained by the SPAD camera, denoted by Y . We have $Y = \mathcal{A}(x)$, where \mathcal{A} is the linear operator mapping the original 2D image x to the 3D measurements.

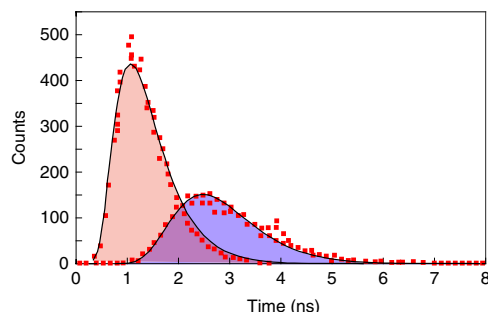


Fig. 3 | Single-pixel temporal histograms of the photon arrivals transmitted through 2.5 cm (red) and 5 cm (blue) of material. Black lines show the best fits with equation (2), with $\mu'_s = 16.5 \text{ cm}^{-1}$ used as a fitting parameter.

The first step is to compute a forward model using equation (2) to simulate light propagation from the input plane to the object plane and then, after masking with a guess estimate (for example, at the first step this can be a simple flat, zero-amplitude distribution), propagation from the object plane to the diffuse medium output. This numerical solution is then compared to the actual measurement by evaluating a cost function. This function is in turn used to modify the shape of the object guess function and is minimized through an iterative process of solving the forward model with the adapted guess target function. Full details of the forward model and iterative cost function minimization are given in the Methods.

Results and discussion

The absorption and scattering parameters of the polyurethane (PU) were measured before the experiment by fitting the temporal diffusion to equation (2). Figure 3 shows the raw data measured at a single pixel for a medium of total thickness 5.0 cm and 2.5 cm: in both cases the coefficients that best fit the experimental data were found to be $\mu_a = 0.09 \text{ cm}^{-1}$ and $\mu'_s = 16.5 \text{ cm}^{-1}$. We then placed objects of various shape, made out of black tape, at the interface between the two slabs of material (as shown in Fig. 1).

Different shapes were tested (the letters 'A' and 'X' and a triangle). Figure 2 shows the results for the three different objects on three different rows. As indicated in the figure, the first columns show the raw data, as recorded directly on the SPAD camera (imaging the output side of the diffusive material), the second column shows the background subtracted data (that is, the data after subtracting out a measurement taken with the laser off), and the third column shows a time-gated image (taken by isolating the first 10 temporal bins of data that rise above the noise floor). As can be seen, there is no discernible information in these time-gated photons and the images actually resemble very closely the total time-integrated images. Reducing the number of time bins selected to perform the gating leads only to a reduction of the overall signal, with no further information on the presence or shape of the occluded object. Finally, the last two columns show the retrieved image of the occluded object and the actual ground truth for the object. It can be seen that the ToF-DOT allows us to correctly assess the presence of the occluded object and also provides a good qualitative agreement with the actual object shape. Whilst the time-integrated or time-gated camera recordings do not show any distinct shadows and thus do not allow us to guess the shape or position of the hidden objects, the method is sensitive to the exact position of the object, as shown in Fig. 4, which shows an example where the 'triangle' is shifted among three different positions while everything else (that is, laser illumination and camera position) remains unchanged. The data for these images were acquired at 1.5 s intervals, showing the potential for tracking of changes within the medium in real time. We note,

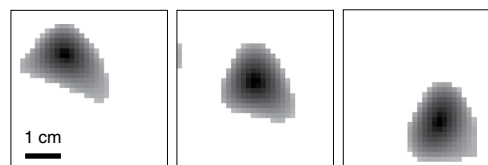


Fig. 4 | Tracking of a hidden object positioned at different positions inside the diffusive medium. Images are 'captured' at 1.5 s intervals.

however, that the retrieval algorithm used to estimate the object shape of interest was performed offline. It required a few minutes to converge for each image on a standard laptop computer, using a Matlab implementation. This could be reduced to sub-second timescales by employing parallel computing methods.

We underline once more that in the operating conditions used here (typical, for example, of a thick sample of human tissue, with an average scattering length of $15\text{--}20 \text{ cm}^{-1}$; ref. ³¹), standard methods such as time gating of ballistic or snake photons⁴ do not allow recognition of the shape of any object considered in our experiment. Indeed, the 5-cm-thick material of our experiment is equivalent to 83 transport mean free paths and this effectively eliminates all ballistic photons.

As can be seen in these results, in all cases the algorithm struggles to reconstruct features such as sharp edges, with a resolution that is limited here to $\sim 0.5 \text{ cm}$. However, we performed a series of numerical simulations based on using the forward model with a hidden object that is composed of two vertical stripes, 0.5 mm thick, 5 mm long and separated by 1 mm. These stripes were embedded in a diffusive medium with the same μ'_s and μ_a as in the experiment at a distance of 2.5 cm from the output surface. We then add noise to the output image to simulate camera noise and then use the data in the ToF-DOT reconstruction algorithm to test the ability to correctly identify the 1 mm gap between two stripes. These tests were performed with increasing spatial resolution (first row in Fig. 5; temporal resolution fixed at 55 ps) and temporal resolution (first row in Fig. 5; spatial resolution fixed at 160×160 pixels). We can see that increasing the spatial or temporal resolution on the camera leads to an increase in the resolution of the final retrieved image of the occluded object. In particular, with 55 ps time bins and 160×160 pixels, feature sizes as small as 1 mm are clearly visible.

On the basis of this finding we performed an experiment aimed at testing our current spatial resolution capability: two vertical stripes (4 mm thickness, 19 mm height) were used, separated by 5, 2 and 1 mm with a fixed pixel count of 32×32 . The results are shown in Fig. 6, which displays the 2D reconstructions. A good qualitative agreement with the ground truth (shaded rectangles) is observed for all separations, although at 1 mm separation, clear artefacts start to appear, for example the two slits are fused together in the lower half. Nevertheless, the retrieval is still able to correctly recognize the existence and overall shape/position of the slits. These measurements therefore highlight current limitations of our approach (difficulty with highly asymmetric features that have details in the sub-mm region) but also the potential to resolve close to mm features in the occluded object.

We note that the 55 ps temporal resolution of the camera corresponds to 1.5 cm in free space. However, in diffusive propagation one should consider the PDW as the wave propagating information through the system and this travels at a much slower speed, requiring several nanoseconds to transit 5 cm, corresponding to a camera resolution of $\sim 0.5 \text{ mm}$. This simplified reasoning seems to agree with our findings that resolution is limited at the millimetre scale. In more detail, if we consider the case in which there is no embedded object in the medium, then each pixel on the camera will record a temporal profile for the photon arrival times at the output that is exactly described by equation (2). Moreover, we know that early

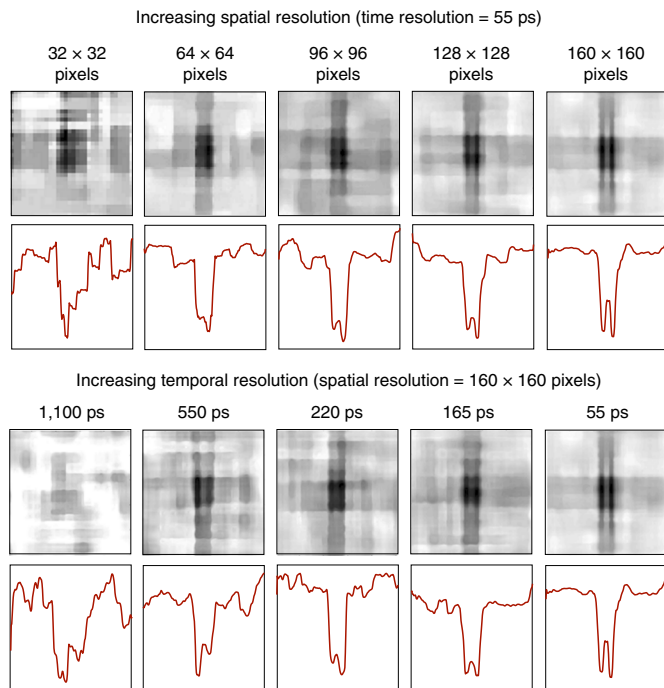


Fig. 5 | Numerical simulations of the reconstruction of a hidden object (0.5 mm thickness, 5 mm height, separated by 1 mm). Top row: the impact of increasing spatial resolution of the camera for a fixed temporal resolution (55 ps). Pixel densities are shown above each figure, illustrating the reconstructed object and a vertical binning of the image to highlight the spatial resolution along the horizontal direction. Bottom row: the impact of increasing the temporal resolution of the camera for a fixed spatial resolution (160 × 160 pixels). The images have not been thresholded (see Methods) in order to highlight the effects of spatial and temporal resolution.

arrival times correspond to photons taking shorter—that is, more direct—paths to the camera, and longer times correspond to photons that travel longer distances due to multiple scattering effects. In the presence of an absorbing object with a spatially extended shape, photon paths that intersect the object will be blocked and will therefore be absent from the final temporal measurement. This in turn will lead to temporal profiles that deviate slightly from equation (2). Furthermore, each spatial pixel on the camera is collecting a different subset of photon paths from the medium, so, in general, the deviations from the perfect temporal profile equation (2) will vary from pixel to pixel. The shape of the object is therefore encoded in this spatially varying temporal information. One can no longer resort to an exact analytical relation to describe the temporal profile modifications at each pixel. These are, however, still fully determined from the solution of the diffusion equation (2) when including the embedded, absorbing object. The retrieval algorithm is therefore iteratively reconstructing the shape of the object that best matches the equation predictions to the measured temporal modifications of the photon signal at each pixel.

Conclusions

We have proposed a computational imaging technique for detecting hidden objects that are completely immersed in a highly scattering medium. The method relies on the full, spatially resolved, ToF information of the photons that are transmitted through the medium and recorded with a photon-counting SPAD camera. The high sensitivity of the camera allows fast acquisition times on the order of 1 s and precise ToF timing. We have shown that, by introducing the full ToF information, we can resolve features in the 1–5 mm range and that this can be improved by increasing both the

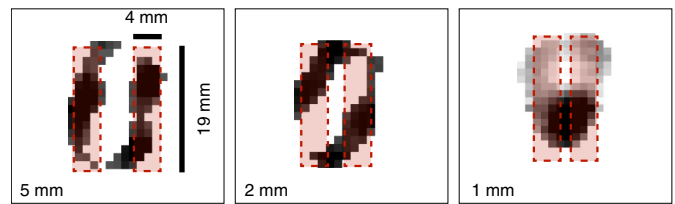


Fig. 6 | Experimental results. Imaging double lines with 32 × 32 pixel density. The images show measurements for three different separations (5, 2 and 1 mm) between the two vertical lines (geometry indicated in the leftmost figure). Shaded areas show the ground truth positions of the vertical lines.

spatial and temporal resolution of the camera. SPAD cameras with high spatial and temporal resolution are currently being developed that also have improved pixel fill factors³² (~60% compared to the ~1% used in these experiments) and thus promise even shorter acquisition times and higher resolutions. We note that intensified charge-coupled device (CCD) cameras are also available with the required 100–200 ps temporal resolution and could be used to perform similar measurements to those shown here.

This work was carried out under the assumption that the medium is homogeneous, which will not in general be true in the case of actual biological tissue or organs. Future work will therefore need to consider the impact of this, for example by including a detailed model of the inhomogeneity in the forward model or by searching for methods for adapting the inverse retrieval.

Online content

Any methods, additional references, Nature Research reporting summaries, source data, statements of code and data availability and associated accession codes are available at <https://doi.org/10.1038/s41566-019-0439-x>.

Received: 9 July 2018; Accepted: 8 April 2019;

Published online: 20 May 2019

References

- Katz, O., Heidmann, P., Fink, M. & Gigan, S. Non-invasive single-shot imaging through scattering layers and around corners via speckle correlations. *Nat. Photon.* **8**, 784–790 (2014).
- Woo, S. et al. Three-dimensional imaging of macroscopic objects hidden behind scattering media using time-gated aperture synthesis. *Opt. Express* **25**, 32722–32731 (2017).
- Satat, G., Tancik, M., Gupta, O., Heshmat, B. & Raskar, R. Object classification through scattering media with deep learning on time resolved measurement. *Opt. Express* **25**, 17466–17479 (2017).
- Wang, L. et al. Ballistic 2-D imaging through scattering walls using an ultrafast optical Kerr gate. *Science* **253**, 769 (1991).
- Konecky, S. D. et al. Imaging complex structures with diffuse light. *Opt. Express* **16**, 5048 (2008).
- Durduran, T., Choe, R., Baker, W. B. & Yodh, A. G. Diffuse optics for tissue monitoring and tomography. *Rep. Prog. Phys.* **73**, 076701 (2010).
- Pifferi, A. et al. New frontiers in time-domain diffuse optics, a review. *J. Biomed. Opt.* **21**, 091310 (2016).
- Shi, L. & Alfano, R. R. *Deep Imaging in Tissue and Biomedical Materials: Using Linear and Nonlinear Optical Methods* (Pan Stanford, 2017).
- Jacques, S. L. Optical properties of biological tissues: a review. *Phys. Med. Biol.* **58**, R37–R61 (2013).
- Delpy, D. T. et al. Estimation of optical pathlength through tissue from direct time of flight measurement. *Phys. Med. Biol.* **33**, 1433–1442 (1988).
- Patterson, B., Chance, M. S. & Wilson, B. C. Time resolved reflectance and transmittance for the non-invasive measurement of tissue optical properties. *Appl. Opt.* **28**, 2331–2336 (1989).
- Jacques, S. L. Time resolved propagation of ultrashort laser pulses within turbid tissues. *Appl. Opt.* **28**, 2223–2229 (1989).
- Hebden, J. C. Evaluating the spatial resolution performance of a time-resolved optical imaging system. *Med. Phys.* **19**, 1081–1087 (1992).

14. Hebden, J. C., Hall, D. J. & Delpy, D. T. The spatial resolution performance of a time-resolved optical imaging system using temporal extrapolation. *Med. Phys.* **22**, 201–208 (1995).
15. Gibson, A. P. & Dehghani, A. Diffuse optical imaging. *Philos. Trans. R. Soc. A* **367**, 3055–3072 (2009).
16. Berg, R., Jarlman, O. & Svanberg, S. Medical transillumination imaging using short-pulse diode lasers. *Appl. Opt.* **32**, 574–579 (1993).
17. Grosenick, D., Wabnitz, H., Rinneberg, H. H., Moesta, K. T. & Schlag, P. M. Development of a time-domain optical mammograph and first in vivo applications. *Appl. Opt.* **38**, 2927–2943 (1999).
18. Boas, D. A. et al. Imaging the body with diffuse optical tomography. *IEEE Signal Process. Mag.* **18**, 57–75 (2001).
19. Torricelli, A. et al. Time domain functional NIRS imaging for human brain mapping. *Neuroimage* **85**, 28–50 (2014).
20. Eggebrecht, A. T. et al. Mapping distributed brain function and networks with diffuse optical tomography. *Nat. Photon.* **8**, 448–454 (2014).
21. Dalla Mora, A. et al. Towards next-generation time-domain diffuse optics for extreme depth penetration and sensitivity. *Biomed. Opt. Express* **6**, 1749–1760 (2015).
22. Pavia, J. M., Wolf, M. & Charbon, E. Single-photon avalanche diode imagers applied to near-infrared imaging. *IEEE J. Sel. Top. Quantum Electron.* **20**, 3800908 (2014).
23. Gibson, A. P., Hebden, J. C. & Arridge, S. R. Recent advances in diffuse optical imaging. *Phys. Med. Biol.* **50**, R1–R43 (2005).
24. Ripoll, J., Nieto-Vesperinas, M. & Carminati, R. Spatial resolution of diffuse photon density waves. *J. Opt. Soc. Am. A* **16**, 1466 (1999).
25. Azizi, L., Zarychta, K., Ettori, D., Tinetti, E. & Tualle, J.-M. Ultimate spatial resolution with diffuse optical tomography. *Opt. Express* **17**, 12132 (2009).
26. Satat, G., Heshmat, B., Raviv, D. & Raskar, R. All photons imaging through volumetric scattering. *Sci. Rep.* **6**, 33946 (2016).
27. Cai, W. et al. Time-resolved optical diffusion tomographic image reconstruction in highly scattering turbid media. *Proc. Natl Acad. Sci. USA* **93**, 13561–13564 (1996).
28. Gariépy, G. et al. Single-photon sensitive light-in-flight imaging. *Nat. Commun.* **6**, 6021 (2015).
29. Yoo, K., Liu, F. & Alfano, R. When does the diffusion approximation fail to describe photon transport in random media? *Phys. Rev. Lett.* **64**, 2647 (1990).
30. Wang, L. V. & Wu, H.-I. in *Biomedical Optics: Principles and Imaging* Ch. 8, 249–281 (Wiley, 2007).
31. Jacques, S. L. Optical properties of biological tissues: a review. *Phys. Med. Biol.* **58**, 5007–5008 (2013).
32. Gyongy, I. et al. A 256×256, 100-kfps, 61% fill-factor SPAD image sensor for time-resolved microscopy applications. *IEEE Trans. Electron. Dev.* **65**, 547 (2018).

Acknowledgements

D.F. acknowledges financial support the Engineering and Physical Sciences Research Council, UK (grants EP/M006514/1 and EP/M01326X/1). Y.W. acknowledges financial support from the Engineering and Physical Sciences Research Council, UK (grants EP/M008843/1 and EP/M011089/1).

Author contributions

A.L. and A.B. performed experiments and data analysis. A.R., F.T. and Y.W. developed the retrieval algorithms and performed data analysis. The project was devised and led by D.F. R.H. developed the SPAD camera. All authors contributed to the preparation of the manuscript.

Competing interests

The authors declare no competing interests.

Additional information

Reprints and permissions information is available at www.nature.com/reprints.

Correspondence and requests for materials should be addressed to D.F.

Publisher's note: Springer Nature remains neutral with regard to jurisdictional claims in published maps and institutional affiliations.

© The Author(s), under exclusive licence to Springer Nature Limited 2019

Methods

Experiment details. A femtosecond laser source is used to deliver 130 fs pulses at 808 nm with a repetition rate of 80 MHz and 1 W average power. A small fraction is reflected off a beamsplitter to an optical constant fraction (OCF) discriminator, while most of the energy is directed towards the scattering medium after the beam has been expanded using a diverging lens. On the other side of the sample the SPAD camera collects the transmitted light having interacted with both the scattering medium and the hidden object placed inside.

The SPAD camera is composed of a 32×32 array of SPAD detectors (100 μm pitch, 8 μm pixel active area diameter), each operating in TCSPC mode. Each individual SPAD can detect the time of arrival of a single photon with a time resolution of ~ 55 ps and impulse response function of 120 ps. The OCF output provides the trigger signal for the SPAD camera. The transmitted light is imaged to the SPAD array through an 8 mm focal length photographic lens (Samyang 8 mm f/3.5 UMC Fish-eye), and the camera is kept at a fixed distance such that the corresponding field of view is covering an area larger than the hidden object dimensions.

Characterization of the scattering medium. The reduced scattering coefficient μ_s' of the polyurethane foam was estimated using the experimental set-up shown in Fig. 1, where the sample consisted of two polyurethane slabs (without any hidden objects). The absorption coefficient μ_a was measured before the experiment using a spectrophotometer, but can also be verified from the same time-resolved measurement used to estimate μ_s' . The reduced scattering coefficient is estimated by comparing the measured temporal broadening and optical delay of a laser pulse with the expected model given by the diffusion approximation, equation (2).

Retrieval algorithm. As described in the Computational retrieval model section, we denote with $Y \in \mathbb{R}^{N \times N \times T}$ the 3D measurements, containing T images of size $N \times N$, and described by the following forward model:

$$Y = \mathcal{A}(x) + W \quad (3)$$

In equation (3), W is a realization of an additive random noise and $\mathcal{A}: \mathbb{R}^{N \times N} \rightarrow \mathbb{R}^{N \times N \times T}$ is the observation operator mapping linearly the hidden object to the 3D measurements. This operator models the acquisition process described in the Computational retrieval model section. The inverse problem defined by equation (3) is ill-posed and requires the development of adapted tools in order to be solved. During recent decades, optimization techniques have been developed to tackle such problems arising in different signal-processing fields^{33,34}. In this context, the unknown object is defined as a minimizer of an objective function composed of a sum of two terms: the data fidelity term related to the forward model and the regularization term incorporating a priori information we have on the target object (for example, piecewise constant image). Therefore, we proceed to minimize a regularized least-squares criterion defined as

$$\underset{x \in \mathcal{C}}{\text{minimize}} \quad \frac{1}{2} \|\mathcal{A}(x) - Y\|_2^2 + \lambda R(\Psi^\dagger(x)) \quad (4)$$

where R promotes sparsity of the target object in a basis induced by the operator Ψ (for example, wavelet basis³⁵, gradient basis³⁶ and so on). Moreover, the amplitude of x is constrained to belong to $\mathcal{C} \subset \mathbb{R}^{N \times N}$. Finally, $\lambda > 0$ is the regularization parameter balancing the importance of the regularization term with respect to the data-fidelity term (least-squares criterion).

To compute the forward propagation $\mathcal{A}(x)$ efficiently, we separate the linear projection into two linear operations: computation of the spatio-temporal intensity field at the depth of the object and propagation of the light field from the object to the observation plane. The former can be performed by an element-wise multiplication between the object, or its current estimate, and each temporal frame of the light field propagated from the illumination point to the object. This only needs to be computed once using equation (2). The latter is computed by convolving the result of the previous operation with the point spread function given in equation (2). Performing these two operations is significantly more efficient than computing the large matrix multiplication representing the full

forward propagation. In addition, to avoid fitting to noise at the edges of the recorded data and consequently causing Fourier transform artefacts when performing the aforementioned convolution operations, the measurements fidelity term $\|\mathcal{A}(x) - Y\|_2^2$ is minimized only over pixels that experience a signal-to-noise ratio in the recorded data Y over a certain threshold. This selection can be performed by multiplication with a selection mask $\mathcal{M}(Y)$. The operator $\mathcal{A}(x)$ is then computed as

$$\mathcal{A}(x) = \mathcal{M}(Y) \times [\Phi(\mathbf{r}_x; t; \mathbf{r}_0, t_0) \odot (\Phi(\mathbf{r}_{\text{out}}; t; \mathbf{r}_{x,0}, t) \times x_T)] \quad (5)$$

where \odot indicates a convolution, $\mathbf{r}_x = (x, y, d_1)$ is the set of 2D spatial coordinates at the illumination-object distance d_1 , \mathbf{r}_0 is the illumination position at the input surface, $\mathbf{r}_{\text{out}} = (x, y, d_1 + d_2)$ is the set of 2D coordinates at the output surface, $\mathbf{r}_{x,0} = (0, 0, d_1)$, $x_T: \mathbb{R}^{N \times N \times T}$ is constructed by repeating the 2D object x in the third dimension T times and $\mathcal{M}(Y)_{i,j,1:T}$ is one if $\sum_k Y_{i,j,k} \geq s$ and zero otherwise, with s being a real positive constant.

It is important to emphasize that both R and Ψ^\dagger can vary with different prior information about x . We use the prior knowledge that the objects we wish to image are both piecewise constant and sparse to then employ a regularization term composed of two different penalty functions $\lambda R(\Psi^\dagger(x)) = \lambda_1 R_1(\Psi_1^\dagger(x)) + \lambda_2 R_2(\Psi_2^\dagger(x))$. The first penalty function induces total-variation (TV) regularization by choosing $\Psi_1^\dagger(x) = [D_h(x), D_v(x)]$, where D_h and D_v represent the horizontal and vertical discrete gradients of the image, respectively³⁶. This regularization term is given by

$$R_1(\Psi_1^\dagger(x)) = \|\mathbf{x}\|_{\text{TV}} = \sum_{i,j} \sqrt{|x_{i+1,j} - x_{i,j}|^2 + |x_{i,j+1} - x_{i,j}|^2} \quad (6)$$

The second penalty function induces sparsity by minimizing the ℓ_1 norm and is given by

$$R_2(\Psi_2^\dagger(x)) = \|\mathbf{x}\|_1 = \sum_{i,j} |x_{i,j}| \quad (7)$$

To solve the minimization problem, we implement a steepest descent algorithm, which iteratively updates a solution $x^{(k)}$ with the gradient of the objective function in equation (4) as $x^{(k)} = x^{(k-1)} - a D^{(k-1)}$, where $D^{(k-1)}$ is the numerical gradient of the objective function evaluated at $x^{(k-1)}$ (ref. ³⁷).

Data availability

All data used in this work are available from <https://doi.org/10.5525/gla.researchdata.642>

Code availability

All codes used in this work are available from <https://doi.org/10.5525/gla.researchdata.642>

References

33. Combettes, P. L. & Pesquet, J.-C. in *Fixed-Point Algorithms for Inverse Problems in Science and Engineering* (eds Bauschke, H. H. et al.) Ch. 10, 185–212 (Springer, 2011).
34. Komodakis, N. & Pesquet, J.-C. Playing with duality: an overview of recent primal-dual approaches for solving large-scale optimization problems. *IEEE Signal Process. Mag.* **32**, 31–54 (2015).
35. Mallat, S. A. *Wavelet Tour of Signal Processing* 2nd edn (Academic Press, 2009).
36. Rudin, L. I., Osher, S. & Fatemi, E. Nonlinear total variation based noise removal algorithms. *Physica D* **60**, 259–268 (1992).
37. Berisha, S. & Nagy, J. G. in *Academic Press Library in Signal Processing* Vol. 4 (eds Chellappa, R. & Theodoridis, S.) 193–247 (Elsevier, 2014).